Influence of finite conductivity on the excitation of phase resonances in metallic surfaces with cavities of circular cross sections

Claudio I. Valencia[1,4] **and Diana C. Skigin**[2,3,5]

[1]*Facultad de Ciencias, Universidad Autónoma de Baja California, Km. 107 Carretera Tijuana-Ensenada, Ensenada, BC 22860, Mexico*
[2]*Grupo de Electromagnetismo Aplicado, Departamento de Física, Facultad de Ciencias Exactas y Naturales, Universidad de Buenos Aires, Buenos Aires, Argentina*
[3]*Consejo Nacional de Investigaciones Científicas y Técnicas, Facultad de Ciencias Exactas y Naturales, Instituto de Física de Buenos Aires (IFIBA), Universidad de Buenos Aires, Buenos Aires, Argentina*
[4]*e-mail: vale@uabc.mx*
[5]*e-mail: dcs@df.uba.ar*

Phase resonances have been investigated in the last few years, not only because of their striking features, such as extremely high quality factor and huge enhancement of the electromagnetic field inside cavities/grooves, but also for their promising applications. However, taking into account that these resonances are more efficiently excited in highly conducting structures, most of the studies have been devoted to explore this phenomenon at wavelengths in the infrared or larger, using different approaches for the boundary conditions. In this paper, we investigate the validity of the perfect conductor approximation and the surface impedance boundary condition to appropriately represent the electromagnetic response of a metallic surface comprising a finite number of subwavelength cavities of circular cross sections. Far- and near-field plots are shown and analyzed in order to investigate the validity ranges and discuss to what extent phase resonances can be excited at shorter wavelengths in these structures.   © 2016 Optical Society of America

OCIS codes: (050.6624) Subwavelength structures; (160.3900) Metals; (290.0290) Scattering.

https://doi.org/10.1364/AO.55.009659

1. INTRODUCTION

In the last two decades, phase resonances have been investigated not only because of their extreme characteristics, but also for their promising applications. Phase resonances are generated by a particular arrangement of the field phases inside the cavities or grooves of a metallic structure. In particular, when the phases in adjacent grooves are opposite to each other, the so-called π mode arises, which corresponds to an extremely high Q resonance accompanied by a significant enhancement of the electromagnetic field inside the cavities [1]. This phenomenon was first reported by Veremey and Mittra in finite arrays formed by cavity-backed apertures [2], and it was later observed in metallic surfaces with a finite number of rectangular grooves [1,3–6] or slits [7,8]. The applications proposed include high-finesse optical filters, light trapping and guiding structures [9–11], corrugated surface antennas [9], channel-selecting devices, actively controlled nano-optic devices, subdiffraction focusing [12], and sensors [13–15].

In a previous paper, we investigated the generation of phase resonances in a perfectly conducting surface with a finite number of cavities of circular cross sections [16] and showed that as the number of grooves is increased, more resonant peaks are produced; these have an extremely high quality factor and are accompanied by an intensification of the internal magnetic field. More recently, the effect introduced by a subwavelength particle located in the vicinity of the surface has also been explored [14], exhibiting the potential of these kinds of structures for a variety of applications. However, by considering a perfectly conducting metal, the results derived are only valid for long wavelengths, typically greater than a few tens of microns.

It is well known that the underlying physical mechanism is the combination of morphological resonances of each individual cavity or slit and the excitation of eigenmodes of multiple-cavity/slit structures [1,4,8,17]. To efficiently excite shape resonances, highly conducting boundaries of the cavities are required, and then, the excitation of phase resonances has mostly been investigated in the millimeter and microwaves regimes under the perfect conductor assumption [4,10,17–19]. Nevertheless, several authors employed different approximate boundary conditions, such as surface impedance and other perturbative approaches [3,5,8,9,20–22], and only a few of them considered a real metal

with ohmic losses [23–25]. However, to the best of our knowledge, none of the reported studies investigated the validity ranges of these approaches.

The purpose of this paper is to explore to what extent phase resonances can be excited at shorter wavelengths and also to investigate the validity of the different approaches to accurately represent the actual metallic structure in connection to phase resonance excitation. For this study we employ the integral method [26], in which we introduce three different boundary conditions at the metallic surface: the perfect conductor (PC) [16], the surface impedance boundary condition (SIBC) [27], and the exact boundary condition (EBC) [28]. We compare the results given by the three approaches for different wavelength ranges and numbers of cavities and establish their validity ranges.

The paper is organized as follows. In Section 2, we present a summary of the integral method, considering the three different boundary conditions: PC, SIBC, and EBC. Comparative results are shown in Section 3, where we present curves of the reflected intensity (far field) as well as the magnitude and phase of the magnetic field within the cavities (near field) for resonant and non-resonant situations. The comparison of the results obtained with the three approaches at different wavelength ranges permits us to evaluate the validity range of each model for the analysis of the phase resonance excitation. Finally, concluding remarks are given in Section 4.

2. INTEGRAL METHOD

The scattering structure consists of M grooves of circular cross sections practiced in an otherwise planar metallic surface (which is invariant along the z direction), as shown in Fig. 1. The cavities have radius R and aperture a, and the distance between centers of adjacent cavities is d. A p-polarized incident beam (magnetic field along the z direction) of frequency ω impinges from vacuum normally onto the structure. Then, if we denote by ψ the z component of the magnetic field, the incident magnetic field can be written in terms of its angular spectrum $A(\alpha)$ as

$$\psi_{\text{inc}}(x, y) = \frac{1}{2\pi} \int_{-k}^{k} A(\alpha) \exp[i(\alpha x - \beta y)]d\alpha, \quad (1)$$

where

$$A(\alpha) = \frac{\psi_0}{\sqrt{2\pi}\sigma} \exp[-\alpha^2 / 2\sigma^2], \quad (2)$$

where $k = \omega/c = 2\pi/\lambda$, λ is the incident wavelength, σ is the angular half-width of the beam, and ψ_0 is a constant. The x and y components of the incident wave vectors, α and β, are related by $\beta = \sqrt{k^2 - \alpha^2}$. In the limit of large $k/(\sqrt{2}\sigma)$, Eq. (1) defines an incident Gaussian beam of spatial half-width $w = \sqrt{2}/\sigma$ [26]. Due to the symmetry of the problem (invariance along the z direction and normal incidence), the problem can be reduced to a scalar one for the unknown complex amplitude of the z component of the magnetic field $\psi(\mathbf{r})$, which satisfies a homogeneous two-dimensional Helmholtz equation,

$$\left[\frac{\partial^2}{\partial x^2} + \frac{\partial^2}{\partial y^2} + \epsilon(\omega)k^2\right]\psi(\mathbf{r}) = 0, \quad (3)$$

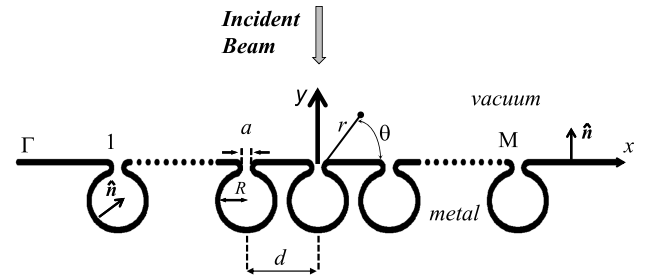where $\epsilon(\omega)$ is the complex dielectric function at the corresponding medium:

Fig. 1. Scheme of the scattering problem under study. The structure comprises several cavities of circular cross sections ruled on a metallic surface. A p-polarized incident beam impinges from a vacuum normally onto the structure. The radii of the cavities R, their apertures a, and the distance between cavities d are indicated.

$$\epsilon(\omega) = \begin{cases} 1 & \text{at vacuum} \\ \epsilon_m(\omega) & \text{at the metal region} \end{cases}. \quad (4)$$

The key point of the integral methods [26,28] is the combination of Green's second integral theorem and Eq. (3). In a vacuum, ψ can be expressed in terms of an integral equation as

$$\psi(\mathbf{r}) = \psi_{\text{inc}}(\mathbf{r}) + \frac{i}{4} \int_{\Gamma} [k\hat{\mathbf{n}} \cdot \hat{\mathbf{u}}(\mathbf{r}|\mathbf{r_s}) H_1^{(1)}[k|\mathbf{u}(\mathbf{r}|\mathbf{r_s})|]\psi(\mathbf{r_s})$$
$$- H_0^{(1)}[k|\mathbf{u}(\mathbf{r}|\mathbf{r_s})|]\varphi(\mathbf{r_s})]dl, \quad (5)$$

where $\mathbf{r}_s$ is a vector-valued function that describes the curve Γ, $\mathbf{u}(\mathbf{r}|\mathbf{r_s}) = \mathbf{r} - \mathbf{r_s}$, $\hat{\mathbf{u}}(\mathbf{r}|\mathbf{r_s}) = \mathbf{u}(\mathbf{r}|\mathbf{r_s})/|\mathbf{u}(\mathbf{r}|\mathbf{r_s})|$, $\hat{\mathbf{n}}$ is a unit vector normal to the profile, and dl is a differential of the arc of Γ. The knowledge of the source function $\psi(\mathbf{r_s})$ and its normal derivative $\varphi(\mathbf{r_s}) = \partial\psi(\mathbf{r})/\partial\hat{\mathbf{n}}|_{\mathbf{r}=\mathbf{r_s}}$ on the boundary permit us to calculate the field at any point in the incidence medium. $H_0^{(1)}$ and $H_1^{(1)}$ are the Hankel functions of the first kind and orders zero and one, respectively. For the metal region, we have

$$0 = \frac{i}{4} \int_{\Gamma} [k_m\hat{\mathbf{n}} \cdot \hat{\mathbf{u}}(\mathbf{r}|\mathbf{r_s}) H_1^{(1)}[k_m|\mathbf{u}(\mathbf{r}|\mathbf{r_s})|]\psi^{(m)}(\mathbf{r_s})$$
$$- H_0^{(1)}[k_m|\mathbf{u}(\mathbf{r}|\mathbf{r_s})|]\varphi^{(m)}(\mathbf{r_s})]dl, \quad (6)$$

where $k_m = \sqrt{\epsilon_m(\omega)}k$, and $\psi^{(m)}(\mathbf{r_s})$ and $\varphi^{(m)}(\mathbf{r_s})$ are the source functions evaluated at the metal side. To calculate the far- and near-field intensities in a vacuum from Eq. (5), $\psi(\mathbf{r_s})$ and $\varphi(\mathbf{r_s})$ are required. These functions are obtained by combining Eqs. (5) and (6) via the boundary conditions on $\mathbf{r_s}$, which establish a relationship between $\psi^{(m)}(\mathbf{r_s})$ and $\varphi^{(m)}(\mathbf{r_s})$ with $\psi(\mathbf{r_s})$ and $\varphi(\mathbf{r_s})$, respectively.

In the following subsections, we summarize the procedures for different boundary conditions.

A. Boundary Conditions
1. Approximate Boundary Conditions
When a perfectly conducting material is assumed, the electromagnetic fields vanish inside the metal. Then, Eq. (6) does not provide additional information to solve the problem, and the boundary condition for p-polarized waves becomes

$$\varphi(\mathbf{r_s}) = 0. \quad (7)$$

Therefore, the problem is reduced to obtain $\psi(\mathbf{r}_s)$ from Eq. (5). Details of the procedure and examples of far and near fields can be found in Refs. [14,16]. From a qualitative point of view, infinite conductivity is a good assumption for metals at wavelengths beyond the infrared. However, the computation of the field values under the PC assumption might not give accurate results even in this region of the spectrum.

In order to improve the metal representation, the surface impedance boundary condition can be employed, which is a more realistic approximation that takes into account the dispersion of the material. This condition provides very good results for metallic structures beyond the infrared zone, both qualitatively and quantitatively. Analogously to the PC case, the problem is reduced to obtain $\psi(\mathbf{r}_s)$ from Eq. (5) [27]. The boundary condition in this case is

$$\varphi(\mathbf{r}_s) = \frac{-ik}{\sqrt{\epsilon_m(\omega)}} \psi(\mathbf{r}_s). \quad (8)$$

Using Eq. (8), the far and near fields can be calculated in the same fashion as in the PC case [14,16].

2. Exact Boundary Condition

When the incident wavelength is below the infrared region, PC and SIBC do not give accurate results for real metals. In this case, exact boundary conditions are required, which can be expressed as

$$\psi(\mathbf{r}_s) - \psi^{(m)}(\mathbf{r}_s) = 0, \quad (9)$$

$$\varphi(\mathbf{r}_s) - \frac{1}{\epsilon_m(\omega)} \varphi^{(m)}(\mathbf{r}_s) = 0. \quad (10)$$

The computation of the electromagnetic fields requires the knowledge of both source functions, $\psi(\mathbf{r}_s)$ and $\varphi(\mathbf{r}_s)$. Then, by setting the observation point $\mathbf{r}$ to be on the profile Γ, Eqs. (5) and (6) become

$$\psi(\mathbf{r}_s) = \psi_{\text{inc}}(\mathbf{r}_s) + \frac{i}{4}\lim_{\tau \to 0}\int_{\Gamma}[k\hat{\mathbf{n}}\cdot\hat{\mathbf{u}}(\mathbf{r}^+|\mathbf{r}_s)H_1^{(1)}[k|\mathbf{u}(\mathbf{r}^+|\mathbf{r}_s)|]\psi(\mathbf{r}_s)$$
$$- H_0^{(1)}[k|\mathbf{u}(\mathbf{r}^+|\mathbf{r}_s)|]\varphi(\mathbf{r}_s)]\mathrm{d}l, \quad (11)$$

$$0 = \frac{i}{4}\lim_{\tau \to 0}\int_{\Gamma}[k_m\hat{\mathbf{n}}\cdot\hat{\mathbf{u}}(\mathbf{r}^+|\mathbf{r}_s)H_1^{(1)}[(k_m|\mathbf{u}(\mathbf{r}^+|\mathbf{r}_s)|]\psi(\mathbf{r}_s)$$
$$- H_0^{(1)}[(k_m|\mathbf{u}(\mathbf{r}^+|\mathbf{r}_s)|]\varphi(\mathbf{r}_s)]\mathrm{d}l, \quad (12)$$

where $\mathbf{r}^+ = \mathbf{r}_s + \tau\hat{\mathbf{n}}$.

B. Field Computation

Once the boundary conditions are applied and the source functions are obtained, the magnetic field can be computed at any point in space using Eq. (5), where the second term corresponds to the scattered field $\psi_{\text{sc}}(\mathbf{r})$.

In the case of the PC boundary condition, Eq. (7) holds, and then only $\psi(\mathbf{r}_s)$ is required. For the SIBC case, the relationship between $\psi(\mathbf{r}_s)$ and $\varphi(\mathbf{r}_s)$ given by Eq. (8) also results in the fact that to compute the scattered field using Eq. (5), only the values of $\psi(\mathbf{r}_s)$ are needed. Finally, in the general case of EBC, both source functions $\psi(\mathbf{r}_s)$ and $\varphi(\mathbf{r}_s)$ must be known to calculate the scattered field.

In all three cases of boundary conditions, far from the structure the scattered field can be written in terms of outgoing waves,

$$\psi_{\text{sc}}(r, \theta) = \exp(i\pi/4)\frac{\exp(ikr)}{(8\pi kr)^{1/2}}R(\theta), \quad (13)$$

where $R(\theta)$ is the scattering amplitude given by

$$R(\theta) = -i\int_{\Gamma}[\mathbf{k}(\theta)\cdot\hat{\mathbf{n}}\psi(\mathbf{r}_s) - i\varphi(\mathbf{r}_s)]\exp\{-i\mathbf{k}(\theta)\cdot\mathbf{r}_s\}\mathrm{d}l, \quad (14)$$

and $\mathbf{k}(\theta) = k(\cos\theta\hat{\mathbf{x}} + \sin\theta\hat{\mathbf{y}})$. In writing Eqs. (13) and (14), we have used the expansion of the Hankel functions for large arguments [29] and the approximation $|\mathbf{u}| \approx r - (\mathbf{k}(\theta)\cdot\mathbf{r}_s)/k$ for the argument of the exponential.

The total normalized scattered power $S(\omega)$ is given by

$$S(\omega) = \frac{P_{\text{scatt}}}{P_{\text{inc}}} = \int I(\theta)\mathrm{d}\theta, \quad (15)$$

where $I(\theta)$ is the differential reflection coefficient, i.e., $I(\theta)\mathrm{d}\theta$ is the fraction of the incident flux that is scattered into the angular region of width $\mathrm{d}\theta$ about the scattering direction θ [26]. For normal incidence, the explicit expression of $I(\theta)$ is

$$I(\theta) = \frac{\sigma|R(\theta)|^2}{(4\pi)^{3/2}k\psi_0^2[1 - (\sigma/2k)^2]}. \quad (16)$$

The integral method has been widely used by many authors to solve a large variety of scattering problems. For instance, in Ref. [30], the authors compared their results with previously published data obtained for different structures, including re-entrant surfaces. The implementation of the integral method used in this work has been successfully employed by the authors to solve the scattering problem of different structures, including rough and multivalued surfaces [31], as those considered in this paper.

In the following section, we show results of the differential reflection coefficient evaluated at $\theta = 0$ ($I(0)$) for the far field, and for the near field we calculate $|\mathbf{H}|^2$ using Eq. (5). The numerical solutions of Eqs. (11) and (12) require a discretization procedure, which consists of replacing the continuous profile Γ by a discrete set of N points [28].

3. RESULTS

As mentioned in Section 1, the main purpose of this paper is to analyze the influence of the finite conductivity of a metal in the excitation of phase resonances.

It is well known that metals are very good conductors for millimeter waves and beyond. However, as the wavelength decreases, metals exhibit a remarkable dispersive response, which is accompanied by a decrease in conductivity and an increment of losses. This drastic change of their dielectric permittivity prevents the scalability of certain electromagnetic phenomena, and, at the same time, allows for new resonant mechanisms, such as surface plasmon excitation. In particular, we are interested in the effect produced by the finite conductivity of a metal in the excitation of phase resonances.

As an introductory example, in Fig. 2 we show curves of reflected intensities as a function of the normalized frequency $kR = (2\pi/\lambda)R$ for structures with different numbers of grooves ($N = 1, 3, 5$). In all the examples of this paper, we
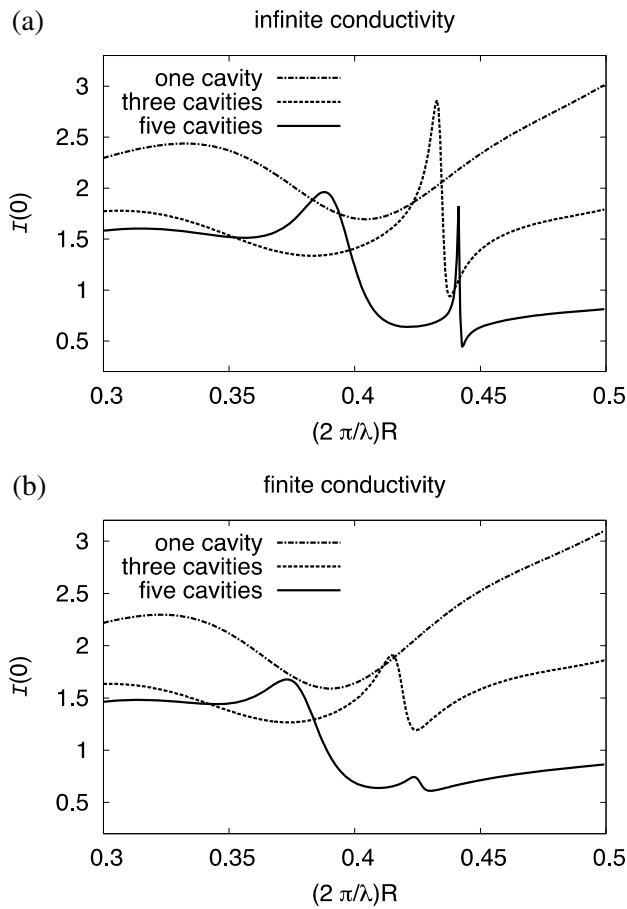
(a)

(b)

Fig. 2. Specular intensity as a function of the normalized frequency for a metallic surface with 1, 3, and 5 cavities. In panel (a), perfectly conducting boundary conditions are imposed (PC case), and in (b), an Al surface is considered (EBC). In the case of the Al surface, the wavelength range considered is $\lambda \in [5.35; 8.38]$ μm.
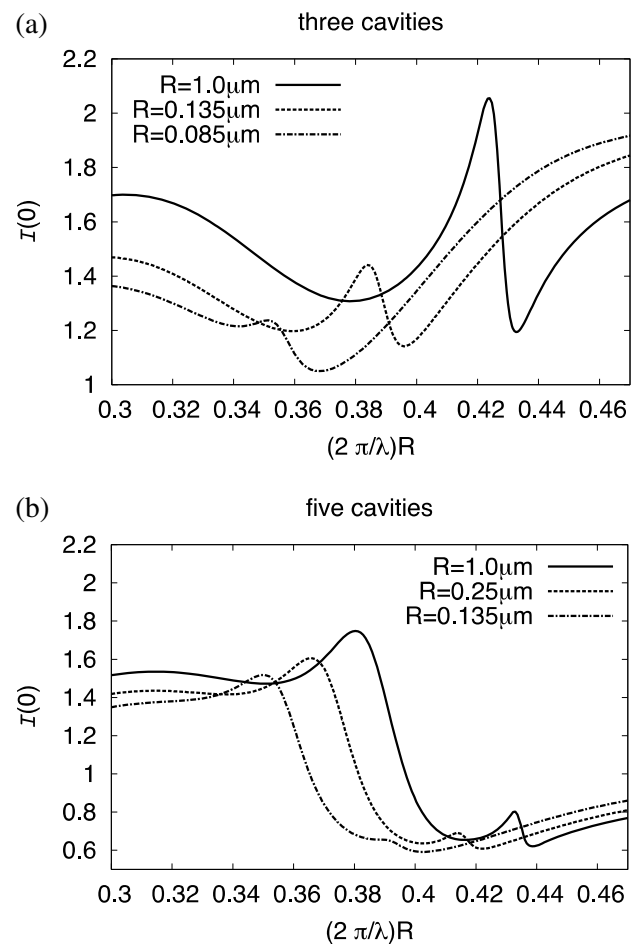
(a)

(b)

Fig. 3. Specular intensity as a function of the normalized frequency for an Al surface with 3 cavities (a) and 5 cavities (b). The exact boundary condition has been considered in the calculation. In each panel, we show curves for different radii, which correspond to different wavelength ranges, as shown in Table 1.

choose $a/R = 0.5787634$, $d/R = 2.1$, and $w/R = 20.0$. In Fig. 2(a) we consider a PC surface, whereas in Fig. 2(b), the grooves are ruled on an aluminum surface modeled as a real metal with losses (the dielectric permittivity of Al has been taken from Ref. [32]). For a single groove in the surface, the specular intensity exhibits a broad minimum associated with the H_{00} mode, which appears due to the aperture practiced in the circular cavity [33]. The addition of closely placed identical cavities produces peaks within the H_{00} mode minimum that arise from the coupling between the electromagnetic fields within individual cavities. This phenomenon has been successfully explained in terms of phase resonance excitation [1,16]. For the three cavities, one resonant peak is obtained, whereas for the five cavities, two peaks can be noticed. The resonances observed for the 3- and 5-groove structures at $kR \approx 0.44$ in Fig. 2(a) are called π resonances, at which the magnetic field phases within adjacent cavities are opposite each other [1]. These resonances appear in the PC as well as in the EBC case [see Fig. 2(b) at $kR \approx 0.42$], although with different characteristics. For instance, notice that the π resonance in the 5-groove case for the PC [Fig. 2(a)] is much higher and has a higher quality than that for the EBC [Fig. 2(b)].

As explained by different authors [1–3,8,17], the generation of phase resonances is based on the distribution of the magnetic field phases within the cavities. The π mode is the highest Q mode among the set of phase resonances that can be excited and is characterized by opposite phases between the magnetic fields of adjacent grooves. Besides, other (lower Q) modes with different phase configurations can also be excited. When the appropriate phase distribution is achieved, the field within the cavities is intensified and, at the same time, a resonant feature is found in the far field. Depending on the kind of structure (reflecting or transmitting, as well as the geometry and distribution of the cavities, etc.) and the incidence conditions, the resonant peak/dip might have a symmetrical or a non-symmetrical shape. In perfectly conducting reflecting structures with rectangular or circular grooves under normal incidence, it was shown that the π mode peak exhibits a non-symmetrical shape, which has been explained as a result of the coupling of the eigenmodes of the structure, which produces a Fano resonance [12], whereas the in-phase peak (the magnetic field phases within the slits are all equal) is basically symmetric

[1,16]. In terms of the quality of these resonances, the perfectly conducting surface exhibits the best performance and produces the narrowest bandwidths.

In the following examples, we illustrate the influence of the finite conductivity and compare the results obtained by the three approaches explained in Section 2, PC, SIBC, and EBC, for the far field (Section 3.A) and for the near field (Section 3.B).

Table 1. R Values and Wavelength Intervals [λ_{min},λ_{max}] Considered for the Results Shown

case	$R[\mu m]$	$\lambda_{min}[\mu m]$	$\lambda_{max}[\mu m]$
A	1.43	19.12	29.94
B	1.2	16.04	25.13
C	1.0	13.37	20.94
D	0.7	9.36	14.66
E	0.40	5.35	8.38
F	0.25	3.34	5.24
G	0.135	1.80	2.83
H	0.1	1.34	2.09
I	0.085	1.14	1.78

A. Far Field

In Fig. 3, we show the evolution of the specular response of the structure as the wavelength decreases (with the corresponding adequacy of $\epsilon_m(\omega)$) for structures with 3 [Fig. 3(a)] and 5 cavities [Fig. 3(b)]. In order to maintain the resonances within the same range of kR, the radii of the cavities are varied accordingly, as shown in Table 1.

The effect of the finite conductivity of a metal as the wavelengths approach the visible range is manifested in all the aspects of the resonances: quality factor, intensity, and spectral location. A significant decrease of the quality of the π resonance is clearly noticed, so in the 3-groove structure, it can be barely visualized for the wavelength range [1.1;1.8] μm (case I, see Table 1). Besides, note that as the wavelengths (and the radius) decrease, the peak shifts to the left side of the H_{00} resonance, i.e., to longer wavelengths relative to the spectral position of the minimum. This is an expected behavior since the finite conductivity allows the penetration of the field in the metal, which enlarges the effective size of the cavities and shifts the resonance to longer wavelengths.

In the case of 5 grooves [Fig. 2(a) for the PC and Fig. 3(b) for the EBC], two peaks can be identified, which correspond to
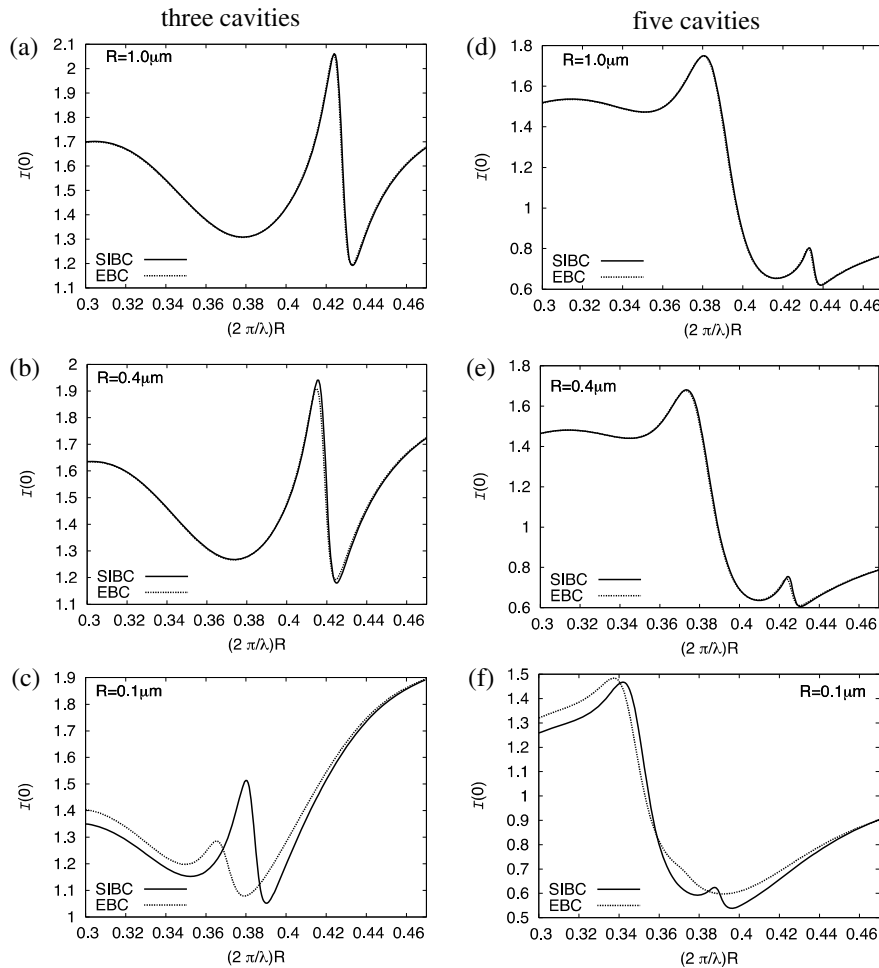

Fig. 4.   Comparison of the specular intensity obtained by the SIBC and the EBC boundary conditions for Al surfaces with 3 and 5 cavities and for different radii of the cavities (and their corresponding wavelength ranges). (a) 3 cavities, case C; (b) 3 cavities, case E; (c) 3 cavities, case H; (d) 5 cavities, case C; (e) 5 cavities, case E; and (f) 5 cavities, case H. The parameters corresponding to each case are listed in Table 1.

different modes allowed by the symmetries of the structure and the incidence conditions [1,8,16]. The high quality of the resonance found at $kR \approx 0.44$ for the PC [Fig. 2(a)], which corresponds to the (+ - + - +) mode, is significantly reduced when a finite conductivity is taken into account, even for wavelengths of the order of tens of microns. However, the lower-quality resonance keeps similar characteristics. Also in this case, the resonant peaks shift to longer wavelengths as the conductivity of the metal decreases.

In view of the results shown above, it becomes evident that the finite conductivity of the metal significantly affects the reflected response of the structure, in particular, the generation of phase resonances. Also, the requirement of a very high conductivity restricts the wavelengths range at which phase resonances can be excited to wavelengths larger than a few microns. For shorter wavelengths, the high Q resonance corresponding to the π mode is almost completely lost.

To get more insight into the physical origin of this behavior, it is essential to explore the near field, particularly the evolution of the magnitude and phase of the magnetic field within the cavities as the conductivity of the metal decreases. Before addressing this issue, in the following example, we analyze to what extent the SIBC is valid to represent the metallic boundaries within the integral method, in connection to the generation of phase resonances. For this purpose, in Fig. 4 we compare the results obtained by the exact approach (EBC) and by the SIBC for different wavelength ranges. It can be noticed that the SIBC and the exact curves almost fully overlap for wavelengths larger than 5 μm [Figs. 4(a), 4(b), 4(d), and 4(e)]. However, for shorter wavelengths, the SIBC curves deviate from the exact values for the 3- as well as for the 5-groove structures. Even though the SIBC curves still exhibit the resonant behavior, neither the shape of the peaks nor their intensity and spectral location are accurately reproduced.

It is important to remark that the relationship between the skin depth (δ) and the minimum distance between cavities ($d_{min} = d - 2R$) is critical when deciding which approach should be applied for the computation of the electromagnetic field. If δ is sufficiently smaller than d_{min}, it is safe to employ the SIBC; on the other hand, if δ is of the order or larger than d_{min}, then the EBC must be used. For instance, for the cases of Figs. 4(a) and 4(d), $\delta \approx 0.2 d_{min}$, and in these cases, the SIBC is appropriate to compute the electromagnetic response. For Figs. 4(b) and 4(e), $\delta \approx 0.45 d_{min}$, and the SIBC curve starts to deviate from the EBC calculation. Finally, for Figs. 4(c) and 4(f), $\delta \approx 1.5 d_{min}$, and it is evident that the SIBC can no longer be used to calculate the scattered fields.

B. Near Field

As mentioned above, as ohmic losses become relevant, the resonant peaks change their characteristics and may even disappear. Since the generation of phase resonances is based on the coupling of resonant modes of the structure, the magnitude and phase distribution of the internal magnetic field is of relevance to investigate this behavior.

In the following examples, we explore the evolution of the electromagnetic field within the cavities as the wavelength approaches the visible range, i.e., as the metal losses become larger. In Fig. 5, we consider a 3-groove structure and show
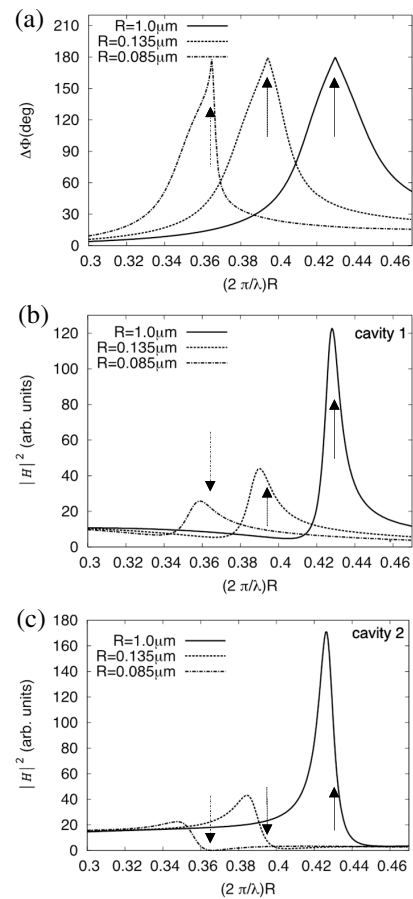

Fig. 5. Magnitude and phase of the magnetic field at the center of each cavity as a function of kR for a 3-groove structure. (a) Phase difference $\Delta\Phi$ between the magnetic fields at the central and the first cavities; (b) $|H|^2$ at the first cavity (which also corresponds to the third cavity due to the symmetry of the incidence configuration); and (c) $|H|^2$ at the second cavity (central). The different curves in each panel correspond to different radii and wavelength ranges, which are listed in Table 1. The arrows indicate the condition $\Delta\Phi = \pi$.

the curves of the magnetic field at the center of each cavity for different wavelength ranges (and the corresponding radii of the cavities, according to Table 1): in (a), we plot the phase difference between the magnetic fields at the first and the central cavities $\Delta\Phi$, in (b) the magnetic field intensity in the first cavity, and in (c) the magnetic field intensity in the central cavity. It can be observed that the condition of opposite phases required for the excitation of the π mode is fulfilled for the three wavelength ranges considered, as shown in Fig. 5(a). However, the decrease of the overall $|H|^2$ at the center of each cavity when the metal losses increase is remarkable. But the key point is that as the losses increase, at the frequency at which the condition $\Delta\Phi = \pi$ is achieved, the values of $|H|^2$ at the central cavity become nearly zero [see Fig. 5(c)]. This implies that instead of having a high Q resonant mode of type (+ - +), we effectively get a (+0+) configuration, which hardly generates an in-phase mode with an extremely low Q [see Fig. 3(a)], not only because the external cavities have the same phase, but also because they have a larger separation from one another, which reduces the coupling.
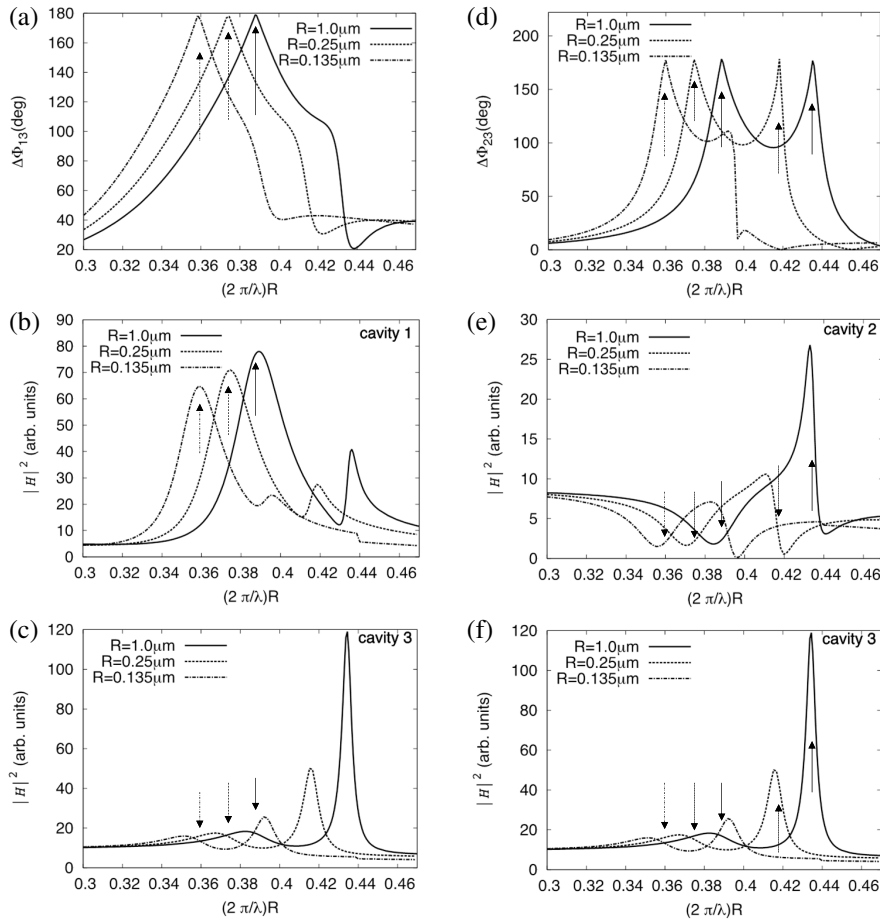
Fig. 6. Magnitude and phase of the magnetic field at the center of each cavity as a function of kR for a 5-groove structure. (a) Phase difference $\Delta\Phi_{13}$ between the central and the first cavities; (b) $|H|^2$ at the first cavity (which also corresponds to the fifth cavity, due to the symmetry of the incidence configuration); (c) $|H|^2$ at the third cavity (central); (d) phase difference $\Delta\Phi_{23}$ between the second and the central cavities; (e) $|H|^2$ at the second cavity (which also corresponds to the fourth cavity); and (f) $|H|^2$ at the third cavity (central). The different curves in each panel correspond to different radii and wavelength ranges, which are listed in Table 1. The arrows indicate the condition $\Delta\Phi = \pi$.

A structure comprising 5 cavities is considered in Fig. 6, where we plot the phase differences $\Delta\Phi_{13}$ [Fig. 6(a)] and $\Delta\Phi_{23}$ [Fig. 6(d)], and the intensities in the centers of the first [Fig. 6(b)], second [Fig. 6(e)] and third cavities [Figs. 6(c) and 6(f)] for the same wavelength ranges considered in Fig. 3(b), where two resonances have been identified in each curve. For case C, these resonances are located at $kR \approx 0.44$ and 0.39. We first analyze the resonance at $kR \approx 0.44$. According to Figs. 6(a) and 6(d), at this resonance, $\Delta\Phi_{13} \approx 0$ and $\Delta\Phi_{23} \approx \pi$, and it corresponds to the π mode or $(+- + -+)$ mode. For the F case, the opposite-phases condition is approximately maintained at the resonance (which is now located at $kR \approx 0.42$), but there is a significant change in the internal field intensities: it decreases significantly in all the cavities, and especially in the second (and fourth) cavities, it becomes negligible. This transforms the phase configuration in type $(+0 + 0+)$, as occurred for the 3-groove case, producing a very low Q resonance due to the weak coupling. If the losses are further increased (case G), not only are the cavity intensities even more reduced, but also, the opposite-phases configuration is almost completely lost, which results in a hardly appreciable resonance [see Fig. 3(b)].

Taking into account the intensities and phases of the internal fields, the resonance located at $kR \approx 0.39$ for case C can be roughly identified with type $(+0-0+)$, which is one of the allowed modes of the ideal structure [12]. However, notice that not only the intensities in cavities 2 and 4 are very small but also the intensity in the central cavity (cavity 3) is low in comparison with the external ones (cavity 1), and this, in turn, contributes to reducing the coupling. As the losses are increased (cases F and G), the intensities at cavities 2 and 4 stay very small, but the relative intensity between the central and the external cavities is similar to case C, as can be noted from Figs. 6(b), 6(c), and 6(e). Therefore, the peak observed in Fig. 3(b) remains even for a wavelength range of a few microns, which corresponds to the small radii of a cavities. As expected, both resonances shift to longer wavelengths (smaller kR) as the losses increase.

C. Spectral Location of the Resonance

It has been shown that the normalized resonant frequency kR_{res} depends on the radii of the cavities, which, in turn, are related to the resonant wavelength and the dielectric permittivity of the
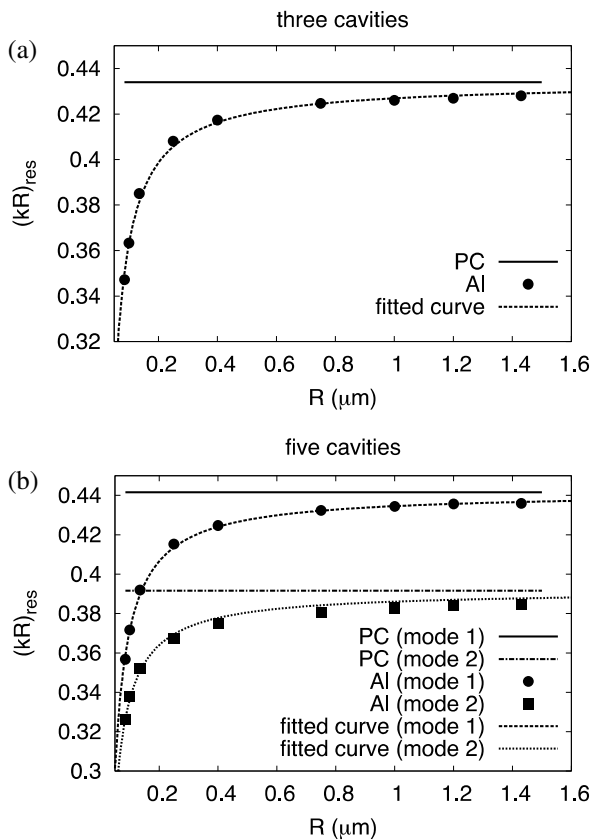
Fig. 7. Normalized resonant frequency kR_{res} as a function of the radius of the cavities R. (a) 3-groove structure and (b) 5-groove structure. The circles correspond to the π resonance $((+ - + - +)$ mode) and the squares to the $(+ 0 - 0 +)$ mode. The fitted curves are also shown.

metal. If we take the maximum enhancement of the field within the central cavity as a criterion for the location of the resonance, we can follow its resonant position as the radii of the cavities increase. In Fig. 7, we show this evolution for the 3- [Fig. 7(a)] and the 5-groove structures [Fig. 7(b)]. The data points correspond to the cases listed in Table 1.

It is evident that as the radii of the cavities increase, the spectral location of each resonance approaches that of the PC case, and this occurs for both the 3- and the 5-cavity structures and, in this case, for both resonant modes. The resonant frequency kR_{res} follows a behavior of the type $kR_{res} = kR_{res}^{PC} - A/R$, where the superscript PC denotes the perfect conductor case and A depends on the number of cavities in the structure and on the resonant mode. The fitted curves are also shown in Fig. 7. For R in μm, in the case of 3 cavities, the fitting parameter is $A = 0.0070951 \ \mu m$, and for 5 cavities, $A = 0.00701272 \ \mu m$ for mode 1 and $A = 0.00553275 \ \mu m$ for mode 2. However, notice that even for the largest radius considered ($R = 1.4 \ \mu m$), i.e., for the wavelength range at which Al conductivity is the highest out of the ranges considered, it is mandatory to use the EBC in order to get accurate results.

4. CONCLUSIONS

We have analyzed the influence of the finite conductivity on the production of phase resonances for structures comprising 3 and 5 cavities of circular cross sections. For this purpose, we implemented three different versions of the integral method, in each of which different approaches for the boundary conditions are considered: perfect conductor, surface impedance boundary condition, and exact boundary condition. In the case of aluminum, the results show that the perfect conductor approximation could appropriately reproduce the field characteristics of phase resonances only for wavelengths larger than 50 μm. For smaller wavelengths up to $\approx 6 \ \mu m$, the SIBC can be safely employed. However, for wavelengths of the order of a few microns or smaller, only the exact boundary condition, which takes into account the actual dielectric permittivity of the metal, can be employed to get an accurate representation of the far and near fields at resonance.

Additionally, we have shown that as the conductivity of the metal decreases, the characteristics of the resonances are modified, basically, their quality factor and spectral location. According to the near-field distribution, we have explained this behavior in terms of the excitation of the different eigenmodes of the whole structure. It was shown that as losses increase, a particular mode can vanish, whereas another mode can be reinforced. This study contributes to understanding the influence of the finite conductivity on the generation of phase resonances. However, further research should be carried out in this topic, i.e., by considering different numbers of cavities, oblique incidence, different cross sections, other metals, etc., in order to be able to exploit phase resonances for concrete applications such as sensors and filters in the near infrared and in the visible range.

REFERENCES

1. D. C. Skigin, V. V. Veremey, and R. Mittra, "Superdirective radiation from finite gratings of rectangular grooves," IEEE Trans. Antennas Propag. **47**, 376–383 (1999).
2. V. V. Veremey and R. Mittra, "Scattering from structures formed by resonant elements," IEEE Trans. Antennas Propag. **46**, 494–501 (1998).
3. J. Le Perchec, P. Quémerais, A. Barbara, and T. López-Ríos, "Controlling strong electromagnetic fields at subwavelength scales," Phys. Rev. Lett. **97**, 036405 (2006).
4. A. Barbara, J. Le Perchec, S. Collin, C. Sauvan, J.-L. Pelouard, T. López-Ríos, and P. Quemerais, "Generation and control of hot spots on commensurate metallic gratings," Opt. Express **16**, 19127–19135 (2008).
5. A. Barbara, S. Collin, Ch. Sauvan, J. Le Perchec, C. Maxime, J.-L. Pelouard, and P. Quemerais, "Plasmon dispersion diagram and localization effects in a three-cavity commensurate grating," Opt. Express **18**, 14913–14925 (2010).
6. M. Beruete, M. Navarro-Cía, D. C. Skigin, and M. Sorolla, "Millimeter-wave phase resonances in compound reflection gratings with subwavelength grooves," Opt. Express **18**, 23957–23964 (2010).
7. M. Navarro-Cía, D. C. Skigin, M. Beruete, and M. Sorolla, "Experimental demonstration of phase resonances in metallic compound gratings with subwavelength slits in the millimeter wave regime," Appl. Phys. Lett. **94**, 091107 (2009).
8. S. Chen, S. Jin, and R. Gordon, "Super-transmission from a finite subwavelength arrangement of slits in a metal film," Opt. Express **22**, 13418–13426 (2014).

9. I. Bendoym, A. B. Golovin, and D. T. Crouse, "The light filtering and guiding properties of high finesse phase resonant compound gratings," Opt. Express **20**, 22830–22846 (2012).

10. A. Enemuo, M. Nolan, Y. Uk Jung, A. B. Golovin, and D. T. Crouse, "Extraordinary light circulation and concentration of s- and p-polarized phase resonances," J. Appl. Phys. **113**, 014907 (2013).

11. Y. Liang, W. Peng, M. Lu, and S. Chu, "Narrow-band wavelength tunable filter based on asymmetric double layer metallic grating," Opt. Express **23**, 14434–14445 (2015).

12. S. Chen, S. Jin, and R. Gordon, "Subdiffraction focusing enabled by a Fano resonance," Phys. Rev. X **4**, 031021 (2014).

13. X. Zhou, J. Fang, D. Yang, X. Zhao, B. Tang, and Z. Liu, "Optical transmission through compound gold surface relief slit arrays," Opt. Express **22**, 1085–1093 (2014).

14. C. I. Valencia and D. C. Skigin, "Phase resonances induced by a subwavelength particle near a surface with two cavities," Appl. Opt. **54**, 7679–7686 (2015).

15. D. C. Skigin and M. Lester, "Refraction index sensor based on phase resonances in a subwavelength structure with double period," Appl. Opt. **55**, 8131–8137 (2016).

16. C. I. Valencia and D. C. Skigin, "Anomalous reflection in a metallic plate with subwavelength grooves of circular cross section," Appl. Opt. **48**, 5863–5870 (2009).

17. A. P. Hibbins, I. R. Hooper, M. J. Lockyear, and J. R. Sambles, "Microwave transmission of a compound metal grating," Phys. Rev. Lett. **96**, 257402 (2006).

18. Y. G. Ma, X. S. Rao, G. F. Zhang, and C. K. Ong, "Microwave transmission modes in compound metallic gratings," Phys. Rev. E **76**, 085413 (2007).

19. M. Pu, C. Hu, C. Huang, C. Wang, Z. Zhao, Y. Wang, and X. Luo, "Investigation of Fano resonance in planar metamaterial with perturbed periodicity," Opt. Express **21**, 992–1001 (2013).

20. D. C. Skigin and R. A. Depine, "Transmission resonances on metallic compound gratings with subwavelength slits," Phys. Rev. Lett. **95**, 217402 (2005).

21. D. C. Skigin and R. A. Depine, "Narrow gaps for transmission through metallic structured gratings with subwavelength slits," Phys. Rev. E **74**, 046606 (2006).

22. J. Le Perchec, P. Quemerais, and A. Barbara, "On light addressing within subwavelength metallic gratings," J. Lightwave Technol. **26**, 638–642 (2008).

23. Y.-B. Chen and M.-J. Huang, "Infrared reflectance from a compound grating and its alternative componential gratings," J. Opt. Soc. Am. B **27**, 2078–2086 (2010).

24. D. Xiang, L.-L. Wang, X.-F. Li, L. Wang, X. Zhai, Z.-H. Liu, and W.-W. Zhao, "Transmission resonances of compound metallic gratings with two subwavelength slits in each period," Opt. Express **19**, 2187–2192 (2011).

25. Y.-B. Chen, M.-J. Huang, and C.-J. Chen, "Directional and hemispherical mid-infrared transmittance through microscale slit arrays on a semi-transparent substrate at normal incidence," J. Quant. Spectrosc. Radiat. Transfer **113**, 1951–1960 (2012).

26. A. A. Maradudin, T. Michel, A. R. McGurn, and E. R. Méndez, "Enhanced backscattering of light from a random grating," Ann. Phys. **203**, 255–307 (1990).

27. C. I. Valencia and R. A. Depine, "Resonant scattering of light by an open cylindrical cavity ruled on a highly conducting flat surface," Opt. Commun. **159**, 254–265 (1999).

28. C. I. Valencia, E. R. Méndez, and B. S. Mendoza, "Second harmonic generation in the scattering of light by two dimensional particles," J. Opt. Soc. Am. B **20**, 2150–2161 (2003).

29. M. Abramowitz and I. A. Stegun, _Handbook of Mathematical Functions_ (Dover, 1970).

30. A. Mendoza-Suárez and E. R. Méndez, "Light scattering by a re-entrant fractal surface," Appl. Opt. **36**, 3521–3531 (1997).

31. C. I. Valencia, D. C. Skigin, and R. A. Depine, "Resonant excitation of the electromagnetic field within a bivalued groove ruled on a highly conducting surface," Opt. Commun. **172**, 125–137 (1999).

32. E. D. Palik, _Handbook of Optical Constants of Solids_ (Academic, 1985).

33. D. Colak, A. I. Nosich, and A. Altintas, "Radar cross-section study of cylindrical cavity-backed apertures with outer or inner material coating: the case of H-polarization," IEEE Trans. Antennas Propag. **43**, 440–447 (1995).